Bahadur J., Melnichenko Y.B., Mastalerz M., Furmann A., Clarkson C.R., 2014. A SANS Study. Energy & Fuels 28 (10), 6336–6344.

Hierarchical Pore Morphology of Cretaceous Shale: A Small-Angle Neutron Scattering and Ultrasmall-Angle Neutron Scattering Study

J. Bahadur,[†] Y. B. Melnichenko,*,[†] Maria Mastalerz,[‡] Agnieszka Furmann,[§] and Chris R. Clarkson[‖]

[†]Biology and Soft Matter Division, Oak Ridge National Laboratory, Oak Ridge, Tennessee 37831-6393, United States

[‡]Indiana Geological Survey, and [§]Department of Geological Sciences, Indiana University, Bloomington, Indiana 47405-2208, United States

[‖]Department of Geoscience, University of Calgary, 2500 University Drive Northwest, Calgary, Alberta T2N 1N4, Canada

ABSTRACT: Shale reservoirs are becoming an increasingly important source of oil and natural gas supply and a potential candidate for CO_2 sequestration. Understanding the pore morphology in shale may provide clues to making gas extraction more efficient and cost-effective. The porosity of Cretaceous shale samples from Alberta, Canada, collected from different depths with varying mineralogical compositions, has been investigated by small- and ultrasmall-angle neutron scattering. The samples come from the Second White Specks and Belle Fourche formations, and their organic matter content ranges between 2 and 3%. The scattering length density of the shale specimens has been estimated using the chemical composition of the different mineral components. Scattering experiments reveal the presence of fractal and non-fractal pores. It has been shown that the porosity and specific surface area are dominated by the contribution from meso- and micropores. The fraction of closed porosity has been calculated by comparing the porosities estimated by He pycnometry and scattering techniques. Although there is no correlation between total porosity and mineral components, a strong correlation has been observed between closed porosity and major mineral components in the studied specimens.

1. INTRODUCTION

The study of pore morphology, sorption characteristics, and potential gas storage capacities of organic-rich shales is important because of potentially significant gas contents of shale gas reservoirs.[1−3] Recent success in extraction of hydrocarbons from tight, unconventional-type reservoirs has stimulated a significant increase in research on self-sourced systems, such as hybrid source rock/reservoir mudstone plays. An assessment of the unconventional hydrocarbon resource potential of source rock/reservoir formations must take advantage of multi-technique approaches to evaluate porosity, organic matter, and mineral matter characteristics.[4]

The pore structure of shale gas reservoirs is difficult to characterize because a major portion of total porosity may be distributed in ultrafine (nano) pores associated with organic matter and clays. Further, shales commonly exhibit a wide pore size distribution, necessitating the use of multiple techniques to investigate the full pore size range. It is important to remember that each technique is based on different principles, and therefore, some differences can be expected even for the same pore ranges. For example, the mercury intrusion porosimetry (MIP) technique measures pore throats, i.e., the largest entrance toward a pore, but not its actual inner size. N_2 and CO_2 gas adsorption techniques can access small pores because of the small size of probing molecules and, hence, are ideal for probing micropores, in contrast to mercury.

A combination of fluid invasion and neutron scattering methods has been used for the characterization of shale samples.[5] Knowledge of the pore size distribution is critical for understanding both fluid/gas flow mechanisms and storage. To minimize exploration risk and evaluate economic feasibility, knowledge of storage and transport mechanisms is necessary, so

that producible resources can be ascertained and long-term production behavior can be evaluated. However, there are insufficient data in the literature that address the relationship between porosity, pore size distribution, and total gas storage/ production capacity in shales as a function of various parameters, such as depth, thermal maturity, organic content, mineralogical composition, etc.

The prediction of shale gas content and potential productivity is complicated by the structurally heterogeneous nature of fine-grained strata and their intricate pore networks, which sometimes appear independent of many geologic factors, including total organic carbon (TOC) content, mineralogy, maturity, and grain size.[6−8] The complexity of shale has made geometrical measurements of pore spaces difficult. Shales are formed by the initial deposition of detrital grains, followed by compaction and diagenesis. Following compaction, the original pore space can be substantially altered by the dissolution of minerals and the growth of cement and pore-filling material. The final result is a very complex structure, which can differ greatly from shale to shale. The pore−matrix interface may not be characterized in terms of regular Euclidean geometric shapes, such as spheres and cylinders. However, there could be some pores in small length scales, where the effect of dissolution is not significant, and those pores can be characterized in terms of the regular Euclidean geometry.

The non-Euclidean morphology of the pores in the shale can be quantified by fractal geometry introduced by Mandelbrot.[9] Estimation of porosity is also important to understand the CO_2

storage potential of shale rock. In recent years, research in CO$_2$ storage in geological formations has increased rapidly. Some favored storage options are saline aquifers, depleted gas and oil reservoirs, or unminable coal seams and organic-rich shales.[10,11] CO$_2$ storage capacity and its long-term retention depend upon the specific surface area provided by micropores and the amount of accessible porosity. The pore morphology and available surface area of rock formations can provide crucial information for exploration of shale for gas and storage of CO$_2$ in organic-rich shales.

In an attempt to elucidate the complex pore structure of shales, researchers have used low-pressure N$_2$ sorption isotherms, He pycnometry, and Hg porosimetry.[6,12−14] However, these fluid invasion techniques provide information only about the accessible pores that are greater in size than the probe molecule. Scattering techniques and, in particular, small-angle neutron scattering (SANS) combined with ultrasmall-angle neutron scattering (USANS) can access pores of size ranging from sub-nanometer to micrometer scale. In contrast to fluid adsorption techniques, scattering techniques can be used to evaluate both accessible and closed pores. Being a non-destructive technique, the same specimens can be used for gas adsorption techniques for complementary information on pore morphology. The SANS/USANS technique can probe the nature of the pore−matrix interface directly. The scattering intensity $I(Q)$ for a fractal object follows a power law with the scattering vector Q; i.e., $I(Q) \sim Q^{-\alpha}$, where the exponent α provides the quantitative measure of inhomogeneity of the fractal object. The scattering intensity in a wide Q range can differentiate between fractal and non-fractal pores.

The porosity in the shale specimens can be calculated using model-dependent analysis of the scattering profiles. The calculated porosity by this method may depend upon the model used for analysis. In addition to this, porosity may be estimated using model-free analysis of scattering profiles by estimating the Porod invariant. It does not depend upon the structure of the two phases but only the porosity and contrast between the pore and matrix of the shale. However, the Porod invariant is extremely sensitive to an incoherent background. Decoupling of the incoherent background and the high-Q flat scattering become very important for precise estimation of the Porod invariant and, hence, porosity.

Recently, shales in the Upper Cretaceous Second White Specks and Belle Fourche formations in central Alberta, Canada, have been investigated using organic petrography, organic geochemistry, and X-ray powder diffraction (XRD); gas adsorption and mercury porosimetry methods have been used for pore characterization.[4] The present study focuses on pore characterization of three representative Cretaceous shale samples from Alberta, Canada, collected from different depths and having different mineralogical composition using SANS and USANS techniques. The samples come from one well location with a limited depth range, so that the maturity of the samples is comparable and not responsible for porosity differences. In addition to pore size distribution, the fraction of closed porosity and available specific surface area in the shale specimens have also been estimated.

2. EXPERIMENTAL SECTION

2.1. Samples. The studied shale samples are from a well (07-19-45-6W5) located in Alberta, Canada. The samples are dark gray to black mudstones with an organic matter content between 2 and 3% (Table 1). Vitrinite reflectance values of 0.78−0.85% indicate mid-level

Table 1. Depth, TOC Content, Total Sulfur (TS) Content, Vitrinite Reflectance (R_o), and He Porosity of the Studied Samples

sample	depth (m)	density (g/cm^3)	TOC (wt %)	TS (wt %)	R_o (%)	He porosity (vol %)
S7	1818.8	2.48	2.04	1.45	0.78	3.2
S9	1822.6	2.71	2.60	3.98	0.85	2.5
S11	1826.6	2.63	2.22	2.85	0.78	3.0

thermal maturity. A Bruker D8 Advance X-ray diffractometer with a Sol-X solid-state detector and a Cu X-ray tube operated at 40 kV and 30 mA was used to identify and quantify mineral phases. Mudstone powders were placed into a large front packed mount (LFPM) and scanned from 2 to 70 using a count time of 2 s per 0.02 step. Multicomponent concentrations were quantified by Rietveld refinements with TOPAS software.[4] Detailed mineralogical and geochemical characteristics of these samples are provided by Furmann et al.[4] Total porosity (vol %) were obtained using helium (He) pycnometry on samples analyzed by the Core Laboratories facility (Houston, TX).[4] Total porosity was calculated from bulk (V_{bulk}) and grain (V_{grain}) volumes. The three representative samples used in the current study are designated as S7, S9, and S11.

2.2. SANS and USANS Experiments. SANS and USANS experiments were performed on powder samples with a grain size of ~0.5 mm. The size of the grains is optimized in such a way that the scattering measurements provide the average information for all orientation of the grains, and the scattering contribution from the grains as well as voids between the grains are negligible in both SANS and USANS regimes. The samples were loaded in aluminum cells of 1.0 mm internal thickness. Thus, the effective thickness of the sample is ~0.5 mm, which helps to minimize multiple scattering. SANS experiments were carried out using the General-Purpose SANS instrument[15] at Oak Ridge National Laboratory (ORNL). The sample detector distances were chosen to cover a wide range of scattering vectors (Q) of $0.002 < Q < 0.5$ Å^{-1}, where $Q = 4\pi\lambda^{-1}\sin(\theta)$ and 2θ is the scattering angle. The wavelength spread $\Delta\lambda/\lambda$ was 0.13. Scattered neutrons were detected using a 1 × 1 m^2 helium-filled two-dimensional (2D) position-sensitive detector with 192 × 192 pixels. The raw 2D data were corrected for the detector pixel efficiency, empty Al cell scattering, and dark current, which represents the ambient radiation background and electronic noise, and azimuthally averaged to produce a one-dimensional (1D) profile $I(Q)$.

USANS measurements were performed at the National Institute of Standards and Technology (NIST), using the BT-5 perfect crystal SANS instrument[16] ($\lambda = 2.4$ Å). The Q range for the USANS measurement was from 4×10^{-5} to 0.003 Å^{-1}. The wavelength spread $\Delta\lambda/\lambda$ was 0.06. The slit-smeared USANS data were desmeared using Lake's method.[17] Application of the GP-SANS and BT-5 instruments in tandem allowed for a broad range of pore sizes, from approximately 4 to 40 000 Å (0.0004−4 μm), to be detected by neutrons.

3. RESULTS AND DISCUSSION

3.1. Calculation of Scattering Length Density (SLD). Parts a and b of Table 2 summarize the content of various mineral components in the shale specimens by weight (determined by XRD) and volume (calculated on the basis of the density) fractions, respectively.

The contrast factor is a very important parameter for quantitative interpretation of SANS data for the shale specimens. The SLD of a multicomponent system may be estimated using the formula[18] below

$$\rho_n = \frac{N_A d}{M} \sum_j p_j \left(\sum_i s_i b_i \right)_j \tag{1}$$

where $N_A = 6.022 \times 10^{23}$ is Avogadro's number, d is the physical density, s_i is the proportion by number of nucleus i in

Table 2. (a) Mineralogical Composition of Studied Samples in Weight Percent as Estimated by Furmann et al.[4] and (b) Mineralogical Composition of Studied Samples in Volume Percent[a]

(a) mineralogical composition of studied samples in weight percent								
sample	quartz (wt %)	albite (wt %)	calcite (wt %)	dolomite (wt %)	ankerite (wt %)	illite (wt %)	kaolinite (wt %)	chlorite (wt %)	pyrite (wt %)
S7	22.22	3.80	12.96	35.83	0.27	17.70	3.43	1.07	2.72
S9	33.45	9.02	3.86	11.54	8.56	20.73	6.03	1.53	5.28
S11	35.10	10.40	0.15	2.46	0.66	36.44	6.51	3.44	4.84
(b) mineralogical composition of studied samples in volume percent								
sample	quartz (vol %)	albite (vol %)	calcite (vol %)	dolomite (vol %)	ankerite (vol %)	illite (vol %)	kaolinite (vol %)	chlorite (vol %)	pyrite (vol %)
S7	20.794	3.596	11.86	31.178	0.2254	15.510	3.259	0.7371	1.3491
S9	34.207	9.329	3.86	10.973	7.810	19.850	6.261	1.1517	2.8617
S11	34.835	10.439	0.1455	2.270	0.5844	33.864	6.559	2.5131	2.5458

[a]Composition in volume percent is obtained from weight percent using the matrix density for each component.

the compound j, p_j is the proportion by molecular number of the compound j in the mixture, and b_i is the coherent scattering amplitude for the nucleus i. It is evident that each shale specimen consists of multiple components (Table 2). If the SLD of each component of the shale is similar within the experimental error, we can assume a two-phase approximation for analysis of SANS data. SANS analysis of two-phase systems is a simplistic approach to estimate the pore morphology of the shale specimens. To estimate the SLD of the individual components of shale, eq 1 was used.

The SLD of each component is shown in Table 3. It is observed that SLDs of major components vary up to 20%. Therefore, in the present case, two-phase approximation is a crude approximation. The organic content in the shale specimens was approximately 2 wt %. The estimated average SLD of the shale will not be affected by the presence of the small amount of organic matter. The organic matter in the shale may be confined to some of the pores, which may affect the contrast between the pore and matrix slightly. The pore size distribution will not be affected by the variation in the SLD of the components if it is assumed that length scales of the individual components do not fall in the size range probed by SANS/USANS. Optical microscopy performed on studied[4] shale specimens indicated that the size of the various components of the shale is larger than the size probed by SANS/USANS. The quantitative analysis of porosity using the average SLD may suffer some degree of error if the pores are not uniformly distributed throughout the shale. The effective SLD of shale specimens has been estimated using eq 1 and is shown in Table 4.

3.2. Interpretation of SANS/USANS Data. In this section, we describe the pore morphology investigated by SANS and USANS techniques. In general, sedimentary rocks possess a heterogeneous structure ranging from mesoscopic macroscopic length scale and often characterized by fractal geometry. The fractal objects possess self-similarity; i.e., the structure of the objects looks similar in all scales. An object that is fractal over a wide length scale can be either mass fractal or surface fractal in nature.[19] For a mass fractal object, the mass or volume is proportional to r^{D_m}, where D_m is known as the mass fractal dimension and varies between 1 and 3. The mass of the three-dimensional Euclidean or non-fractal object scales as r^3. For a surface fractal object, the self-similarity exists only on the surface of the object. In this case, the surface area scales with r^{D_s}, where D_s is known as the surface fractal dimension. The value of D_s lies between 2 and 3. It is noteworthy that, for a smooth Euclidean object, the surface area scales with r^2. For an

extremely rough surface, the fractal dimension is close to 3. It is noteworthy that, because of the power law correlation in the fractal systems in real space, the SANS/USANS profile also manifests a power law behavior[20,21] i.e., $I(Q) \sim Q^{-\alpha}$. For a mass fractal object, the mass fractal dimension (D_m) is equal to the value of α. For a surface fractal object, the surface fractal dimension (D_s) is equal to $6 - \alpha$.

Schmidt et al.[19] has shown that power law scattering intensity can be explained theoretically if the scattering occurs on a particular polydisperse distribution $f(r)$ of randomly oriented independently scattering particles of any shape: $f(r) \sim r^{-(1 - D_s)}$. Recently, Radlinski et al.[22] have demonstrated that the polydisperse spherical pore (PDSP) model can be used to accurately describe various aspects of the micro-architecture of sedimentary rock.

The combined SANS/USANS profiles of the shale specimens are shown in Figure 1. The scattering profiles show an extended linear regime on a log–log scale.

The combined SANS/USANS profiles of the shale specimens are shown in Figure 1. The scattering profiles show an extended linear regime on a log–log scale. The slope of the linear region is ∼3.1 for all of the specimens, indicating the surface fractal nature of shale specimens over a wide length scale. In other words, the pore–matrix remains surface fractal in a wide Q range. It is clear from Figure 1 that the scattering profiles in the log–log scale deviate from linear behavior at high Q, with the scattering at high Q being relatively flat. This clearly indicates that the structure of the shale specimens no longer remains fractal in nature below a threshold size. The flat scattering at high Q is termed as background (BKG). It is thought to be Q-independent and originates from incoherent scattering from hydrogen atoms bound in the organic matter and sorbed water present in the rock. The PDSP model with a flat background BKG is therefore adopted to fit the scattering profiles.

The scattering intensity predicted by the PDSP model may be written as

$$I(Q) = (\rho_1 - \rho_2)^2 \frac{\varphi_f}{\overline{V}} \int_{R_{min}}^{R_{max}} V_r^2 f(r) F_{sph}(Qr) \, dr + BKG$$

(2)

where $\overline{V} = \int_0^\infty V_r f(r) \, dr$ is the average pore volume, ϕ_f is the porosity of the specimens, and $f(r)$ is the power law pore size distribution and can be written as

$$f(r) = \frac{r^{-(1+D_s)}}{(R_{min}^{-D_s} - R_{max}^{-D_s})/D_s}$$

(3)

Table 3. Chemical Formula and SLD of Mineral Components of the Specimens Studied

sample	chemical formula	empirical formula	$\sum S_i b_i$ (cm)	SLD ($\times 10^{10}$, cm^{-2})	MW (g)	density (g/cm^3)
quartz	SiO_2	SiO_2	1.5755	4.184	60.085	2.65
albite	$NaAlSi_3O_8$	$NaAlSi_3O_8$	6.596	3.968	263.02	2.62
calcite	$CaCO_3$	$CaCO_3$	2.8755	4.6887	100.09	2.71
dolomite	$CaMg(CO_3)_2$	$CaMg(CO_3)_2$	5.8185	5.415	184.40	2.85
ankerite	$Ca(Fe,Mg,Mn)(CO_3)_2$	$CaFe_{0.6}Mg_{0.3}Mn_{0.1}(CO_3)_2$	5.971	5.17	206.39	2.97
illite	$(K,H_3O)(Al,Mg,Fe)_2(Si,Al)_4O_{10}[(OH)_2,(H_2O)]$	$K_{0.6}(H_3O)_{0.4}Al_{1.3}Mg_{0.3}Fe^{2+}_{0.1}Si_{3.5}O_{10}(OH)_2 \cdot (H_2O)$	8.2082	3.593	389.34	2.83
kaolinite	$Al_2Si_2O_5(OH)_4$	$Al_2Si_2O_5(OH)_4$	5.2467	3.194	258.16	2.61
chlorite	$(Mg,Fe)_5Al(Si_3Al)O_{10}(OH)_8$	$Mg_{3.75}Fe_{1.25}Si_3Al_2O_{10}(OH)_8$	12.585	4.584	595.22	3.6
pyrite	FeS_2	FeS_2	1.5144	3.80	119.98	5.0

$(\rho_1 - \rho_2)^2$ is the contrast factor, where ρ_1 is the SLD of the matrix and ρ_2 is the SLD of the pores. The experiment was performed on powdered specimens; i.e., specimens were not dispersed in either liquid or gas phase, and hence, ρ_2 for empty pores is assumed to be zero. Some pores may also contain organic matter, and the SLD of the organic matter is quite small compared to the SLD of the shale matrix. Hence, the effective contrast between the shale matrix and pores filled with organic matter is slightly different compared to that between empty pores and the shale matrix. This effect reduced further if the fraction of pores filled with organic matter is small. Therefore, it is assumed that the contrast factor in the present case is simply the square of the SLD of the matrix.

The fitting of the PDSP model fit to the data has been depicted in Figure 1. The estimated parameters are given in Table 4, and the calculated pore size distribution is depicted in Figure 2. The fractal dimension D_s is found to be 2.9 for all of the specimens, indicating a highly rough pore−matrix interface. In general, lower and upper fractal cutoffs are determined from deviation from the linear behavior of the scattering profile in a log−log scale at high and low Q, respectively. In the present experiment, the lower cutoff has been estimated accurately because of observed deviation of scattering profiles from linear behavior at high Q. However, the low Q scattering data are not sufficient to determine the upper cutoff precisely because no deviation of the scattering profile from linear behavior is observed. From fitting of the experimental data by the PDSP model, we could estimate a lower limit of fractal upper cutoff (Table 4).

It is evident from Tables 1 and 4 that there is a large difference in porosity calculated by the PDSP model and He pycnometry technique. We also attempted to use a model-free Porod invariant (PI) method to estimate the porosity using eq 4.

$$Q_{inv} = \int_0^\infty Q^2 I(Q) \, dQ = 2\pi^2 (\rho_1 - \rho_2)^2 \varphi_f (1 - \varphi_f) \qquad (4)$$

Q_{inv} is the Porod invariant and has been calculated from the experimental profile. It is important to discuss here that $I(Q)$ in eq 4 should be corrected for the incoherent background. Estimation of porosity for the shale specimens having substantial microporosity is very sensitive to precise estimation of the incoherent background. We first assume that flat high-Q scattering is due to the incoherent background ($\sim$0.11 cm^{-1}). However, we will show later that flat high-Q scattering cannot be attributed only as a result of the incoherent scattering. Porosity calculated by the Porod invariant is 1 order of magnitude lower than the He porosity for all of the specimens (Table 4). It important to mention here that porosity measured by the SANS/USANS technique is expected to be greater than or equal to He porosity for a given length scale because of the inaccessibility of helium to closed pores. Therefore, under-estimation of porosity by both the PDSP model and PI method indicates exclusion of some pores, which contributes to scattering at high Q and is not taken into account.

To understand the discrepancy between porosities measured by scattering and He pycnometry, we looked at the fit of the scattering profiles with the PDSP model in three different Q ranges. The low-Q regime of the scattering profiles is shown in Figure 3.

The PDSP model fit the experimental data quite well in the low-Q regime. The intermediate-Q regime of the scattering profiles is shown in Figure 4. It is evident that the PDSP model

Table 4. Estimated SLD and Porosity Estimated by the Porod Invariant for Shale Specimens and Parameters for the PDSP Model for the Linear Region of the Scattering Profiles

sample	SLD ($\times 10^{10}$, cm^{-2})	porosity (PI) (%)	PDSP porosity, ϕ_f (%)	D_s	lower cutoff (Å)	upper cutoff (Å)	BKG
S7	4.01	0.65	0.44	2.9	50	>100000	0.11
S9	4.05	0.54	0.43	2.9	50	>100000	0.11
S11	3.6	0.65	0.53	2.9	50	>100000	0.11
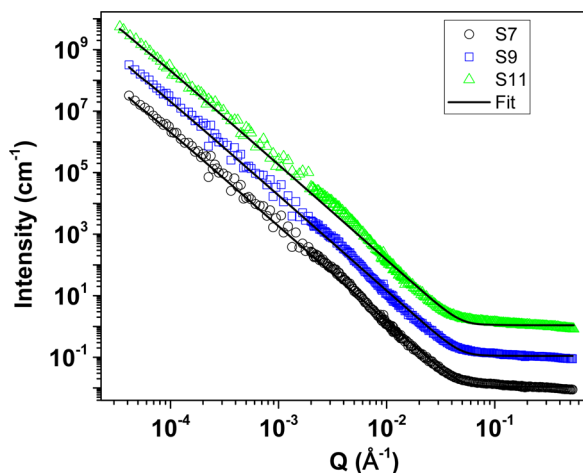
Figure 1. Combined SANS/USANS profiles of shale specimens. The solid line represents the PDSP model fit to the data. Scattering profiles are scaled vertically for the sake of clarity. The scale factor for S7, S9, and S11 was 0.1, 1.0, and 10, respectively.
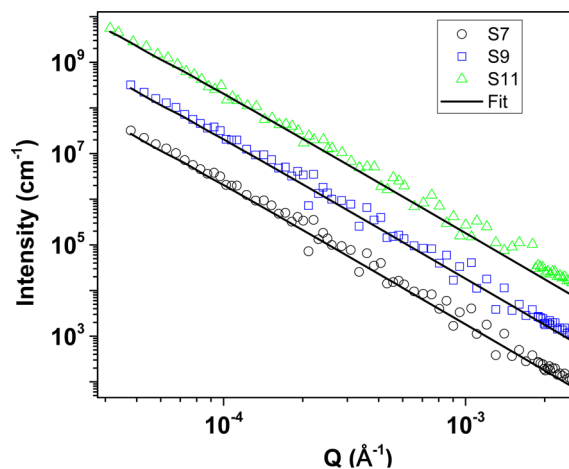
Figure 3. Zoomed view of the low-Q regime of the scattering profiles. The PDSP model provides a good fit. The profiles are scaled vertically for clarity. The scale factors for S7, S9, and S11 are 0.1, 1.0, and 10.0, respectively.
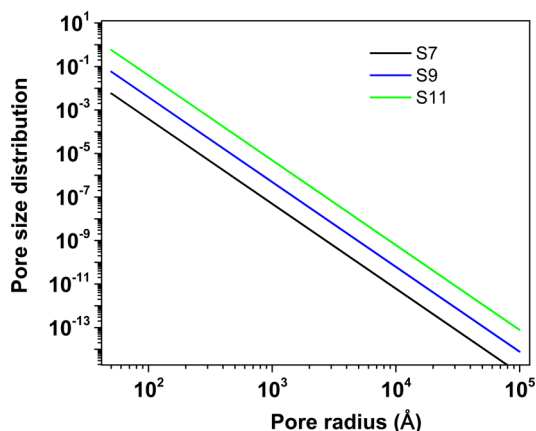
Figure 2. Estimated pore size distribution from the PDSP model. The profiles are scaled vertically for clarity. The scale factors of pore size distributions for S7, S9, and S11 are 0.1, 1.0, and 10.0, respectively.

fit deviates from the experimental data quite significantly. This deviation is attributed to the additional scattering from some non-fractal pores and characterized by Euclidean geometry. These pores are referred to herein as non-fractal meso-/macropores. The deviation is more pronounced if scattering profiles are plotted in the Porod representation, i.e., $I(Q) \times Q^4$ versus Q (Figure 4b). The scattering profiles manifest Q^{-4} scattering behavior in the intermediate-Q range, indicating the presence of smooth meso-/macropores in the shale specimens. It is pertinent to mention here that the International Union of Pure and Applied Chemistry (IUPAC) terminology[23] for macro-, meso-, and micropores has been well-established in the literature and is adopted in the present work. According to this, pore diameters of micropores are less than 2 nm and the pore

diameters of mesopores lie between 2 and 50 nm. The pores having diameters greater than 50 nm are called macropores.

The high-Q part of the scattering profiles is shown in Figure 5. In contrast to the PDSP model fit, the scattering profile is not a constant in this Q regime. In fact, the scattering intensity varies with Q but remains relatively flat. Hence, it cannot be assumed entirely because of the incoherent background. Indeed, this Q-dependent flat scattering originates from micropores present in the shale specimens. The PDSP model adopted for fitting the data before does not account for these micropores and, hence, underestimates the porosity.

We adopted a more general model to account for fractal and non-fractal meso-/micropores to fit the experimental profiles. The expression of scattering intensity for this case can be written as below

$$I(Q) = I_{\text{fractal}}(Q) + I_{\text{mesopores}}(Q) + I_{\text{micropores}}(Q) + \text{BKG} \quad (5)$$

The expression for the intensity because of a fractal distribution of pores is already given in eq 1. Scattering contribution because of non-fractal meso-/micropores is given by

$$I_{\text{meso/micro}}(Q) = (\rho_1 - \rho_2)^2 \frac{\varphi}{\overline{V}} \int V_r^2 D(r) F_{\text{sph}}(Qr)\, dr \quad (6)$$

where $D(r)$ is the log-normal distribution of the meso-/micropores, $F_{\text{sph}}(Qr)$ is the form factor for spherical pores, $(\rho_1 - \rho_2)^2$ is the contrast factor for meso-/micropores, and ϕ is the volume fraction of the meso-/micropores. V_r is the volume of pores having radius r. We have assumed a spherical shape of the meso-/micropores for the fitting for simplicity. In a real situation, the shape of the pores could be much more complicated, for which no analytical expression for the form factor is available. It is important to note at this point that the meso- and micropores may not be distributed uniformly in the
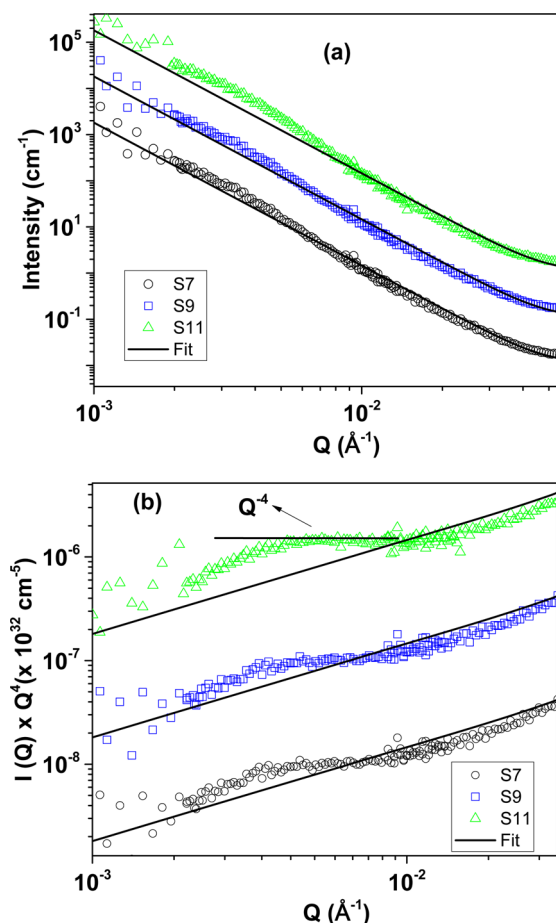
Figure 4. Zoomed view of the intermediate-Q regime of the scattering profiles: (a) $I(Q)$ versus Q and (b) $I(Q) \times Q^4$ vs Q. The profiles are scaled vertically for clarity. The scale factors for S7, S9, and S11 are 0.1, 1.0, and 10.0, respectively.
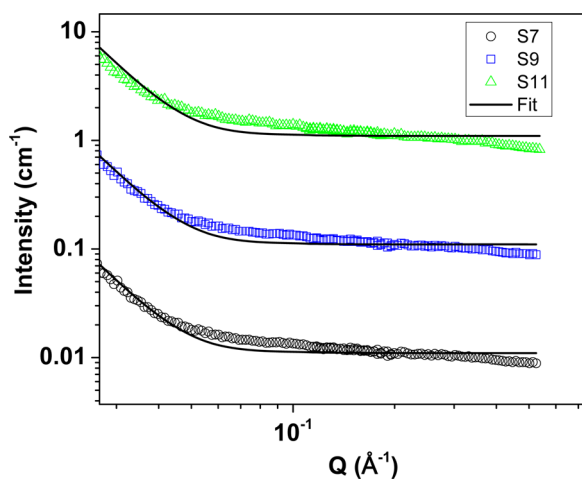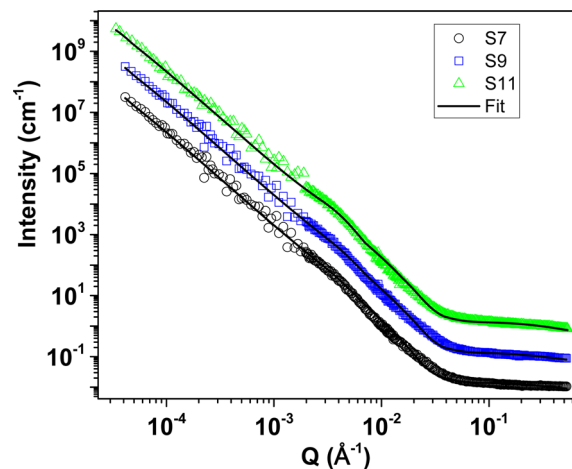

Figure 5. Zoomed view of the high-Q regime of the scattering profiles. The profiles are scaled vertically for clarity. The scale factors for S7, S9, and S11 are 0.1, 1.0, and 10.0, respectively.

shale matrix. It is possible that these pores could be localized in or between certain components of the shale. In this case, the average SLD of the shale specimens cannot be used for quantitative analysis of the meso-/micropores.

The fitted scattering profiles with the revised model are shown in Figure 6. A zoomed view of the fit to the scattering

profiles in intermediate- and high-Q regimes is shown in Figures 7 and 8, respectively.

Figure 6. Scattering profiles fitted with the revised model. The profiles are scaled vertically for clarity. The scale factors for S7, S9, and S11 are 0.1, 1.0, and 10.0, respectively.
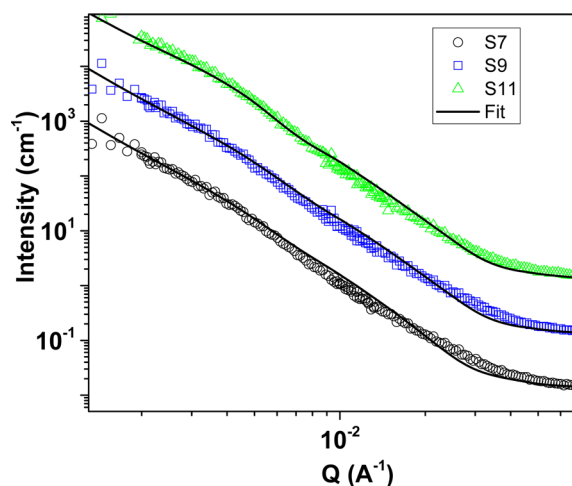

Figure 7. Zoomed view of the intermediate-Q regime of the scattering profiles. Additional scattering has been taken into account in the revised model. The profiles are scaled vertically for clarity. The scale factors for S7, S9, and S11 are 0.1, 1.0, and 10.0, respectively.

It is evident from Figures 6−8 that fitting with the revised model to the experimental data is quite satisfactory. Estimated pore size distributions for three types of pores (fractal, mesopores, and micropores) are depicted in Figures 9−11, respectively. Estimated pore size distributions possess partial overlapping as far as the IUPAC definition of macro-, meso-, and micropores is concerned. It is important to mention here that pores described by the PDSP model are surface fractal in nature and may be termed as fractal pores. Fractal pores possess size (diameter) in the range from 24 nm to 2 μm. Therefore, in addition to all macropores, some mesopores are fractal in nature too. Similarly, the estimated non-fractal mesopore size distribution possesses both meso- and macropores. There is a slight overlap of mesopores in the estimated micropore size distribution from SANS analysis.

The estimated background from eq 5 reduces considerably once the Q-dependent flat scattering as a result of micropores is taken into account. The revised background estimated for all of
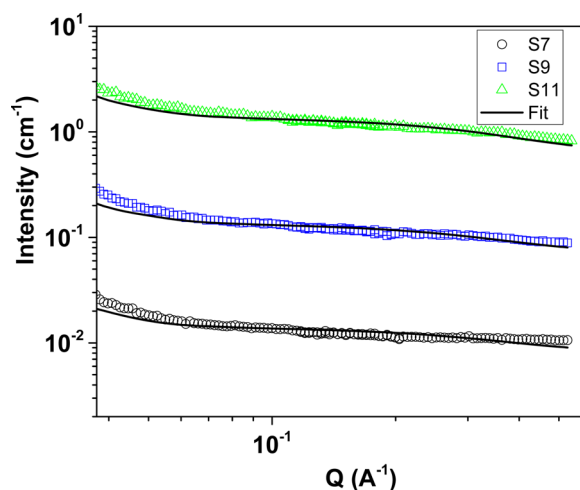
Figure 8. Zoomed view of the high-Q regime of the scattering profiles. The Q dependence of the scattering profile has been taken into account by considering the micropores. The profiles are scaled vertically for clarity. The scale factors for S7, S9, and S11 are 0.1, 1.0, and 10.0, respectively.
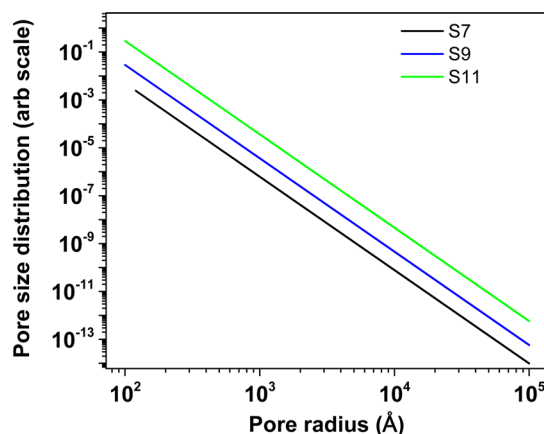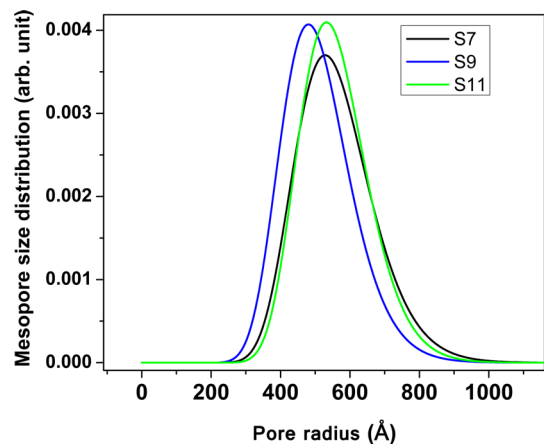

Figure 9. Estimated fractal pore size distribution from SANS analysis. The profiles are scaled vertically for clarity. The scale factors for S7, S9, and S11 are 0.1, 1.0, and 10.0, respectively.

Figure 10. Estimated mesopore pore size distribution from SANS analysis.

the specimens is shown in Table 5. The Porod invariant method is again adopted for evaluating porosity in the
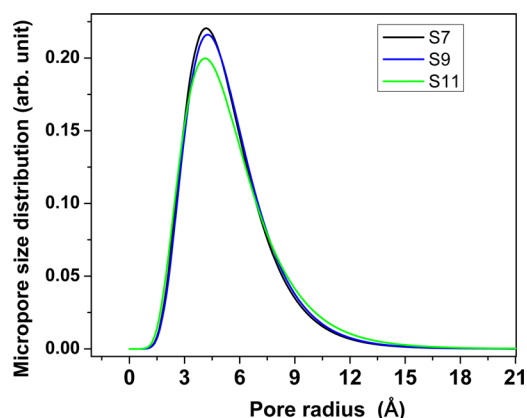

Figure 11. Estimated micropore pore size distribution from SANS analysis.

specimens as a model-free check. Now, the reduced background was subtracted from the experimental scattering profiles (Table 5) before calculating the Porod invariant. The porosity values, estimated using the reduced background, are shown in Table 5. Porosities for the different specimens obtained from SANS/USANS are now closer to those obtained from helium pycnometry. It is interesting to note that the amount of porosity associated with fractal pores is small, implying that the majority of porosity comes from non-fractal micro-/mesopores. This result is also confirmed by gas adsorption measurements[4] on these samples.

If we compare the total porosity measured by He pycnometry (Table 1) and SANS analysis (Table 5), it is observed that porosity estimated by SANS analysis is higher compared to He porosity, indicating the presence of closed pores in shale specimens. The fraction of closed porosity has been estimated by calculating the difference between porosity obtained by SANS and He pycnometry techniques. The fraction of closed porosity for each specimen is given in Table 5.

It is observed from Table 5 that total porosity is different for each sample. Variations in thermal maturation of organic matter have been suggested as a cause for variation of porosity in shale because of the conversion of organic matter to gaseous and liquid hydrocarbons.[24−28] However, in the present case, thermal maturity does not vary significantly, and hence, the variation in porosity is not related to thermal maturity. The changes in porosity with depth might occur because of variations in organic and mineral composition. Although some studies have shown that porosity increases with organic matter,[4,28,29] such a relationship is not observed for the present studied samples because of insignificant variation in TOC contents. In the present study, neither maturity nor organic matter content are primary controls on porosity. Thus, it may be concluded that mineral composition is an important control on porosity and pore size distribution in this sample suite. Scanning electron microscopy (SEM) performed on shale samples has indicated the presence of intra- and interparticle pores within and among minerals.[30−32] We suggest that the variation of porosity in the current study is related to the intra- and interparticle pores of constituent minerals.

It is evident from Tables 1 and 5 that the fraction of closed pores increases with increasing depth. However, the difference in depth is only ~8 m, which translates to a very small pressure difference in the subsurface. Therefore, we believe that the

Table 5. Estimated Parameters from Multi-scale Modeling of the SANS Data

sample	D_s	fractal pore size distribution r_{min} (Å)	r_{max} (Å)	mesopore size distribution median radius (Å)	polydispersity index	micropore size distribution median radius (Å)	polydispersity index	BKG	fractal porosity (%)	porosity (PI) (%)	fraction of closed pores (%)
S7	2.9	120	>100000	500	0.20	5	0.40	0.085	0.44	4.0	20
S9	2.9	100	>100000	500	0.20	5	0.40	0.075	0.43	3.7	32
S11	2.9	100	>100000	500	0.18	5	0.44	0.068	0.53	4.8	37

systematic variation in closed porosity is related to variation in the mineralogical component. There is no strong correlation between total porosity and clay mineral content in the shale; however, a significant correlation is observed between closed porosity and mineral contents as shown in Figure 12.
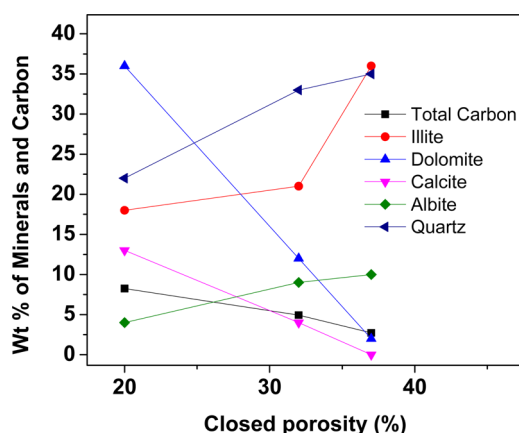

Figure 12. Cross-plot of closed porosity (vol %) and mineral content (wt %) for three samples.

The shallowest sample 7 has the least amount of quartz and clays and the largest amount of carbonates, and it is possible that carbonates (and dolomite in particular) result in a larger proportion of open pores compared to quartz or clays. We think that X-ray tomography and electron microscopy in conjunction with SANS/USANS could provide crucial information to evaluate the complex pore structure, such as micro-/mesoporosity and their size distribution, quantitatively in the shale specimen. In particular, the phase distribution of meso-/micropores in shale is quite important for quantitative analysis and will be the subject of future work.

To evaluate the CO_2 sequestration capabilities of shale, information about available surface area is very important. The specific surface area as a result of fractal pores depends upon the scale of measurement. The specific surface area for probe size "r" is calculated from the pore size distribution as the sum of surface areas of all pores, of radius larger than r, divided by the sample volume

$$\frac{S(r)}{V} = n_v \int_r^{R_{max}} A_r f(r') \, dr' \qquad (7)$$

where n_v is the average number of pores per unit volume; $n_v = \phi_f / \overline{V}_r$. $S(r)/V$ is the specific surface area of pores with radius larger than r, and $A_r = 4\pi r^2$.

The available surface area as a result of fractal pores is shown in Figure 13. It is evident that the maximum specific surface area as a result of fractal pores is less than 0.1 m²/g, which is not significant as far as sequestration of CO_2 is concerned.
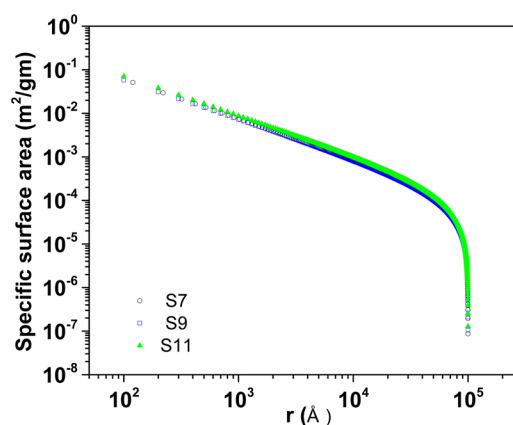

Figure 13. Specific surface area (m²/g) as a result of fractal pores as a function of scale.

A Porod level has been observed in the scattering profiles of the specimens in the intermediate-Q range (Figure 4). This Porod level originates from surface scattering from non-fractal meso-/macropores. The specific surface area has been estimated from the observed Porod level as below

$$\frac{S}{V} = \frac{\pi}{Q_{inv}} \lim_{Q \to \infty} (I(Q)Q^4) \qquad (8)$$

Q_{inv} is estimated using integration of the experimental profile. The estimated specific surface area as a result of non-fractal meso-/macrospores is shown in Table 6.

Table 6. Specific Surface Area as a Result of Non-fractal Meso-/Micropores

sample	specific surface area (m²/g) (mesopores)	specific surface area (m²/g) (micropores)
S7	0.93	19.3
S9	1.01	19.3
S11	1.25	20.1

It is evident that no Porod level is observed for the micropores because of the high-Q limit. However, the scattering profiles have been extrapolated to higher Q to estimate the Porod level because of micorpores. Using eq 8, the specific surface area as a result of micropores has been estimated (Table 6).

From Figure 13 and Table 6, it is concluded that the specific surface area in the present specimens mostly comes from meso-/micropores. The specific surface area as a result of micropores is large because of the small pore size.

4. CONCLUSION

We investigated the pore morphology in Cretaceous shale samples from Alberta, Canada. SANS/USANS analysis reveals a

hierarchical pore structure having a length scale from the sub-nanometer to micrometer scale. The fractal-type pore model cannot represent the experimental data at all length scales. Detailed SANS data analysis provides evidence for the presence of non-fractal macro-/meso-/micropores in the studied specimens. The flat high-Q scattering is dominated by scattering from micropores. Estimation of the precise background is crucial for extracting total porosity using the Porod invariant method. The significant porosity in these specimens comes from meso-/micropores, which are non-fractal in nature. The average SLD of the shale specimens cannot be used for quantitative analysis of the meso-/micropores if they are confined in a certain component of the shale. This is because of the uncertainty in the estimation of the contrast factor, which hinders the quantitative analysis of micro-/mesoporosity. It has also been argued that variation in total porosity is due to intra- and interparticle porosity associated with the constituent mineral components.

Although there is no strong correlation between total porosity and the mineralogical composition of the shale specimens, there is a strong correlation between closed porosity and mineralogical composition. It has been established that the fraction of closed pores increases with the percentage of certain mineral. There is a large specific surface associated with micropores in our sample suite, which can be used in CO_2 sequestration. It is useful to use electron microscopy, in particular, transmission electron microscopy (TEM), to estimate the chemical composition of the phases where meso-/micropores are distributed. With knowledge of the matrix of the meso-/micropores in the shale specimens, one can calculate the contrast factor for these pores, which will facilitate direct estimation of the volume fraction and number density of meso-/micropores from SANS measurement.

■ AUTHOR INFORMATION

Corresponding Author
*Telephone: +1-865-576-7746. E-mail: melnichenkoy@ornl.gov.

Notes
The authors declare no competing financial interest.

■ ACKNOWLEDGMENTS

■ REFERENCES

(1) Montgomery, S. L.; Jarvie, D. M.; Bowker, K. A.; Pallastro, R. M. *AAPG Bull.* **2005**, *89*, 155−175.
(2) Pollastro, R. M. *AAPG Bull.* **2007**, *91*, 551−578.
(3) Ross, D. J. K.; Bustin, R. M. *Bull. Can. Pet. Geol.* **2007**, *55*, 51−75.
(4) Furmann, A.; Mastalerz, M.; Schimmelmann, A.; Pedersen, P. K.; Bish, D. *Mar. Pet. Geol.* **2014**, *54*, 65−81.
(5) Mastalerz, M.; He, L.; Melnichenko, Y. B.; Rupp, J. A. *Energy Fuels* **2012**, *26*, 5109−5120.
(6) Yang, Y.; Aplin, A. C. *Mar. Pet. Geol.* **1998**, *15*, 163−175.
(7) Dewhurst, D. N.; Aplin, A. C.; Sarda, J. P. *J. Geophys. Res.* **1999**, *104*, 29261−29274.
(8) Chalmers, G. R. L.; Bustin, R. M. *Int. J. Coal Geol.* **2007**, *69*, 288−304.
(9) Mandelbrot, B. B. *The Fractal Geometry of Nature*; Freeman: New York, 1977.
(10) Hitchon, B.; Gunter, W. D.; Gentzis, T.; Bailey, R. T. *Energy Convers. Manage.* **1999**, *40*, 825−843.
(11) Holloway, S. *Energy Convers. Manage.* **1997**, *38*, 241−245.
(12) Eseme, E.; Littke, R.; Kroos, B. M. *Mar. Pet. Geol.* **2006**, *23*, 715−734.
(13) Clarkson, C. R.; Freeman, M.; He, L.; Agamalian, M.; Melnichenko, Y. B.; Mastalerz, M.; Bustin, R. M.; Radlinski, A. P.; Blach, T. P. *Fuel* **2012**, *95*, 371−385.
(14) Clarkson, C. R.; Solano, N.; Bustin, R. M.; Bustin, A. M. M.; Chalmers, G. R. L.; He, L.; Melnichenko, Y. B.; Radliński, A. P.; Blach, T. P. *Fuel* **2013**, *103*, 606−616.
(15) http://neutrons.ornl.gov/gpsans/.
(16) Barker, J. G.; Glinka, C. J.; Moyer, J. J.; Kim, M. H.; Drews, A. R.; Agamalian, M. *J. Appl. Crystallogr.* **2005**, *38*, 1004−1011.
(17) Lake, J. A. *Acta Crystallogr.* **1967**, *23*, 191−194.
(18) Radlinski, A. P. In *Reviews in Mineralogy and Geochemistry*; Wenk, H.-R., Ed.; Mineralogical Society of America (MSA): Chantilly, VA, 2006; Vol. 63: Neutron Scattering in Earth Sciences, Chapter 14, pp 363−397.
(19) Schimidt, P. W. *J. Appl. Crystallogr.* **1991**, *24*, 414.
(20) Texeira, J. *J. Appl. Crystallogr.* **1988**, *21*, 781−785.
(21) Freltoft, T.; Kjems, J. K.; Sinha, S. K. *Phys. Rev. B: Condens. Matter Mater. Phys.* **1986**, *33*, 269.
(22) Radlinski, A. P.; Mastalerz, M.; Hinde, A. L.; Hainbuchner, M.; Rauch, H.; Maron, M.; Lin, J.-S.; Fan, L.; Thiyagarajan, P. *Int. J. Coal Geol.* **2004**, *59*, 245−271.
(23) Singh, K. S. W.; Everett, D. H.; Haul, R. A. W.; Moscou, L.; Pierotti, R. A.; Rouquerol, J.; Siemieniewska, T. *Pure Appl. Chem.* **1985**, *57*, 603−619.
(24) Curtis, M. E.; Cardott, B. J.; Sondergeld, C. H.; Rai, C. S. *Int. J. Coal Geol.* **2012**, *103*, 26−31.
(25) Jarvie, D. M.; Hill, R. J.; Ruble, T. E.; Pollastro, R. M. *AAPG Bull.* **2007**, *91*, 475−499.
(26) Loucks, R. G.; Reed, R. M.; Ruppel, S. C.; Hammes, U. *AAPG Bull.* **2012**, *96*, 1071−1098.
(27) Mastalerz, M.; Schimmelmann, A.; Drobniak, A.; Chen, Y. *AAPG Bull.* **2013**, *97* (10), 1621−1643.
(28) Modica, C. J.; Lapierre, S. G. *AAPG Bull.* **2012**, *96*, 87−108.
(29) Haynes, R. J.; Naidu, R. *Nutr. Cycling Agroecosyst.* **1998**, *51*, 123−137.
(30) Ross, D. J. K.; Bustin, R. M. *Mar. Pet. Geol.* **2009**, *26*, 916−927.
(31) Slatt, R. M.; O'Brien, N. R. *AAPG Bull.* **2011**, *95*, 2017−2030.
(32) Tian, H.; Pan, L.; Xiao, X.; Wilkins, R. W. T.; Meng, Z.; Huang, B. *Mar. Pet. Geol.* **2013**, *48*, 8−19.